Am J Transl Res 2026;18(8):7075-7091
www.ajtr.org /ISSN:1943-8141/AJTR0175229

Original Article

Integrated multi-omics atlas reveals PTM-driven signaling and immunologic remodeling in a mouse model of age-related subclinical hypothyroidism

Kun Xu[1], Qing Zhou[2]

[1]*Department of General Surgery, Jiangsu Province Hospital of Chinese Medicine, Affiliated Hospital of Nanjing University of Chinese Medicine, Nanjing 210029, Jiangsu, China;* [2]*Department of Ophthalmology, Children's Hospital of Nanjing Medical University, 72 Guangzhou Road, Gulou District, Nanjing 210008, Jiangsu, China*

Received July 7, 2026; Accepted August 12, 2026; Epub August 15, 2026; Published August 30, 2026

Abstract: Objective: Age-related subclinical hypothyroidism (AR-SCH) profoundly impairs thyroid structural and functional integrity in the elderly, yet the systemic molecular architecture driving AR-SCH pathogenesis remains poorly understood. This study aimed to construct a comprehensive multi-omic atlas of the AR-SCH mouse thyroid. Methods: Global proteomics, site-specific N-glycoproteomics, and phosphoproteomics were integrated to profile thyroid tissues from AR-SCH and control mice. Results: In total, 6,666 proteins, 2,476 site-specific N-glycans, and 11,929 phosphorylation sites were identified. Global proteomics revealed a widespread reduction of functional proteins (81.7% downregulated), primarily associated with cytoskeletal structural remodeling and tissue degeneration under AR-SCH conditions. N-glycoproteomics identified altered fucosylation and reduced N-glycosylation associated with extracellular-matrix organization and local immune-related processes. Furthermore, an extensive hypophosphorylation trend (91.53% downregulated sites) was associated with suppression of intracellular signaling cascades, possibly involving autophagic clearance and perturbed apoptotic homeostasis. Conclusion: Multi-omics integration suggests an interconnected network as a convergent hallmark of AR-SCH progression, characterized by cytoskeletal reconfiguration, immune regulation shifts, and signaling attenuation that synergistically contribute to systemic thyroid decline, offering a therapeutic window for preserving endocrine homeostasis.

Keywords: Thyroid aging, N-glycoproteomics, phosphoproteomics, proteomics, mouse

Introduction

Aging is a complex biological process characterized by a progressive decline in tissue integrity and physiologic function [1, 2]. Recent studies have highlighted that immune aging is closely associated with age-related tissue degeneration and functional decline [3]. In the endocrine system, the thyroid gland is highly susceptible to age-related degeneration, which frequently manifests as morphologic atrophy, altered hormone synthesis, and a blunted response to thyrotropin [4, 5]. Clinically, these functional deteriorations contribute to an important rising incidence of autoimmune thyroid disorders and high prevalence of subclinical hypothyroidism in the elderly [6-8]. Given the pervasive role of thyroid hormones in regulating systemic metabolism, thermogenesis, and cardiovascular homeostasis, age-related thyroid dysfunction severely compromises healthspan and exacerbates cardiovascular mortality [5, 9, 10].

The fundamental mechanisms driving thyroid aging are increasingly recognized through the lens of geroscience, encompassing hallmarks such as loss of proteostasis, cellular senescence, and mitochondrial dysfunction [11]. Recent advances in high-throughput transcriptomics and single-level proteomics have provided initial insight into age-related transcriptional dysregulation and protein expression dynamics across multiple organs, including the thyroid [5, 12-14]. However, the correlation between mRNA and actual functional protein levels is often limited, especially during aging [15]. More importantly, the functional status of

https://doi.org/10.62347/PQYE9899

proteins is heavily dictated by post-translational modifications (PTMs) - such as glycosylation and phosphorylation - that govern protein folding, cellular localization, and signal transduction [16, 17]. To date, a systemic, multi-layered mapping of the aging thyroid proteome and its dynamic PTMs remains an important knowledge gap.

Glycosylation and phosphorylation are two highly dynamic PTMs essential for maintaining thyroid follicular homeostasis and immune tolerance [17, 18]. N-glycosylation is an important determinant of extracellular matrix organization, immune recognition, and proper folding of thyroid proteins like thyroglobulin [19]. Notably, aberrant glycosylation patterns, such as altered immunoglobulin G core fucosylation, have been strongly implicated in mediating antibody-dependent cell-mediated cytotoxicity and driving autoimmune thyroid diseases [20, 21]. Concurrently, protein phosphorylation acts as a regulatory element for intracellular signaling cascades. Dysregulated kinase activity and aberrant phosphorylation signaling are known to directly compromise autophagic clearance and promote cellular senescence and apoptosis, which are important drivers of tissue aging [22-26].

To delineate systematically the molecular architecture of thyroid aging, we herein performed an integrated, deep multi-omics analysis on young and age-related subclinical hypothyroidism (AR-SCH) mouse thyroids. By combining data-independent acquisition (DIA) global proteomics with high-precision site-specific N-glycoproteomics and phosphoproteomics, we identified 6,666 proteins, 2,476 site-specific N-glycans, and 11,929 phosphorylation sites, capturing an unprecedented, multi-dimensional landscape of the aging thyroid. Our integrated analysis unravels a widespread age-associated reduction of functional proteins and outlines a interconnected network involving cytoskeletal structural remodeling, immune homeostasis shifts, and coordinated apoptosis/autophagy signaling variations. This integrated multi-omics atlas provides a high-resolution mechanistic framework for understanding the age-related decline in thyroid function and offers candidate targets for translational interventions in geriatric endocrinology.

Materials and methods

Animals

An age-related subclinical hypothyroidism (AR-SCH) model was established using female C57BL/6 mice, as 20-month-old mice are physiologically equivalent to 60-year-old humans. Overall, 28-week-old C57BL/6 mice were obtained from Beijing Vital River Laboratory Animal Technology Co., Ltd. and raised in the SPF-grade animal room of Nanjing Medical University (IACUC 1808004). The mice were housed with free access to food and water under a 12 h light/dark cycle, with all experimental supplies fully sterilized before use. Upon reaching 20 months of age, mouse serum levels of T3, T4, and serum thyrotropin (TSH) were quantified by enzyme-linked immunosorbent assay (ELISA). Mice with elevated TSH and normal FT4 levels were defined as successful AR-SCH model animals.

Hematoxylin-eosin (HE) staining

Unilateral thyroid tissues were surgically harvested, fixed in 4% paraformaldehyde (PFA) (Biosharp, BL539A), paraffin-embedded, and cut into 5 μm-thick sections for hematoxylin-eosin (H&E) staining (YuanYe, R32933). All tissue sections were visualized under a light microscope (BX53, OLYMPUS) at 200× magnification for morphologic observation.

ELISA-based determination of thyroid peroxidase and thyroglobulin antibody levels

Approximately 1 mL of blood was extracted from the posterior ocular venous plexus of each anesthetized mouse. After the blood samples rested at room temperature for 30 min, the serum was isolated by centrifuging for 15 min at 3,000 rpm and then stored at -80°C for later hormone analysis. Finally FT4 (ASB, EK6868), FT3 (KeyGEN, KGC1066), TSH (CUSABIO, CSB-E05116m), and anti-thyroglobulin antibody (TGAB) (CUSABIO CSB-E09543m) were measured by ELISA method on a full-wavelength microplate reader (Thermo Scientific, Multiskan GO).

Histology and immunofluorescence

After deparaffinization, thyroid sections were subjected to heat-induced antigen retrieval in

10 mM sodium citrate buffer (pH 6.0) via microwave treatment for 20 min (Beyotime, P0083). The sections were incubated with rabbit anti-TPO primary antibody (1:100, CST, 12829). After rinsing with deionized water and PBS, sections were blocked with 5% goat serum for 60 min, followed by incubation with goat anti-rabbit IgG (H+L) secondary antibody (1:100, Invitrogen, A21202). 4',6-diamidino-2-phenylindole (DAPI) (Beyotime, C1006) was applied for DNA counterstaining. All immunofluorescence images were acquired using a Nikon ECLIPSE Ti confocal microscope with consistent parameter settings.

Protein sample preparation

Thyroid tissue samples were lysed in ice-cold lysis buffer containing 8 M urea, 50 mM Tris-HCl, 75 mM NaCl, 1% phosphatase inhibitor cocktail, and protease inhibitor cocktail. Tissue homogenization was performed on ice, followed by ultrasonic cavitation for disruption. Lysates were centrifuged at 20,000×g for 1 h at 4°C, and supernatants were collected for protein quantification using the Bradford assay. For proteolysis, equal amounts of protein were reduced with 5 mM dithiothreitol (DTT) at 55°C for 35 min, followed by alkylation using 15 mM iodoacetamide (IAA) in the dark for 20 min. Excess DTT was added to quench unreacted IAA, and samples were diluted fivefold with 25 mM Tris-HCl. Trypsin was added at a ratio of 10 ng per μL protein, and digestion was carried out overnight at 37°C. The reaction was acidified with trifluoroacetic acid (TFA) to a final concentration of 0.5%, followed by desalting. An aliquot of the purified peptides was used for global proteomic analysis by liquid chromatography-tandem mass spectrometry (LC-MS/MS).

Enrichment of intact N-glycopeptides

Intact N-glycopeptides were enriched using hydrophilic interaction chromatography (HILIC) following a published protocol with minor modifications [27]. In brief, desalted peptides were dissolved in 0.1% TFA and mixed with activated HILIC beads at a peptide-to-resin mass ratio of 1:50. The mixture was incubated at room temperature for 2 h with continuous rotation. After two sequential washes with 80% acetonitrile (ACN) containing 0.2% TFA, N-glycopeptides were eluted with 0.1% TFA. Eluted fractions were vacuum-dried and desalted before LC-MS/MS analysis.

Phosphopeptide enrichment

Phosphorylated peptides were enriched using titanium ion-immobilized metal affinity chromatography (Ti^{4+}-IMAC) as previously described with optimizations [28]. Lyophilized peptides were reconstituted in loading buffer and incubated with Ti^{4+}-IMAC beads at room temperature for 30 min. Beads were sequentially washed with wash buffer 1 (50% ACN, 3% TFA, 200 mM NaCl) and wash buffer 2 (30% ACN, 0.1% TFA). Phosphopeptides were then eluted twice with elution buffer 1 (10% ammonium hydroxide) and once with elution buffer 2 (80% ACN). Eluates were combined, vacuum-dried, and stored for mass spectrometry analysis.

LC-MS/MS analysis

The liquid chromatography-mass spectrometry (LC-MS) analysis was performed using an Orbitrap Fusion Lumos mass spectrometer (Thermo Fisher Scientific) coupled with an Easy-nLC 1200 nano-liquid chromatography system. Peptide separation was performed on an analytical column (15 cm × 75 μm, IonOpticks). Global proteome samples were separated with a 60-min LC gradient, whereas phosphoproteome and N-glycoproteome samples were subjected to a 95-min LC gradient.

For global proteome and phosphoproteome, data were acquired in data-independent acquisition (DIA) mode. Full-scan MS spectra were acquired at a resolution of 120,000 over m/z 350-1500, with automated gain control (AGC) set to 250% and maximum injection time of 50 ms. MS/MS spectra were generated using higher-energy collisional dissociation (HCD) at normalized collision energy (NCE) of 30% and detected at 30,000 resolution with dynamic maximum injection time. For N-glycoproteome, MS1 spectra were acquired from m/z 400-1200 at 120,000 resolution, with precursor charge states 2-7, AGC set to standard, and maximum injection time of 100 ms. MS/MS spectra were acquired in data-dependent mode (DDA) with 1.6 m/z isolation window and stepped collision energy HCD (20%, 30%, 40%) at 60,000 resolution.

Database search and protein identification

For global proteome and phosphoproteome, raw DIA files were processed using Spectronaut (v19.9) against the Mus musculus UniProt

reviewed database (downloaded March 2025). Up to two missed tryptic cleavages were allowed. Carbamidomethylation (C) was set as a fixed modification; oxidation (M) was set as a variable modification. False discovery rate (FDR) was controlled to 1% at peptide-spectrum match, peptide, and protein levels. Direct^{DIA} search was applied with peptide length restricted to 7-52 amino acids; other parameters were set as default. For phosphoproteome analysis, phosphorylation (S/T/Y) was added as an additional variable modification.

For the N-glycoproteome, raw files were analyzed using Glyco-Decipher (v1.0.5) against the Mus musculus UniProt reviewed database (downloaded March 2025). Search parameters included: full tryptic specificity; precursor mass tolerance, 10 ppm; fragment mass tolerance, 20 ppm; up to three missed cleavages. Fixed modification: carbamidomethylation (C). Variable modification: oxidation (M). FDR for glycopeptide-spectrum matches was controlled below 1%.

Bioinformatics and statistical analysis

Only proteins, phosphorylation sites, or site-specific N-glycans that were quantified in ≥ 60% of samples per group were retained. Missing values were imputed with 0.8 times the minimum observed intensity, followed by log2(intensity+1) transformation. To eliminate expression-dependent bias, phosphorylation site intensities were normalized by subtracting the log2(protein intensity+1) value from the corresponding log2(phosphorylation site intensity+1) value; unadjusted log2(phosphorylation site intensity+1) values were used when cognate proteins were undetected in global proteomics. Differentially regulated molecules were defined by fold change (FC) > 1.5 or FC < 0.67 and *P*-value < 0.05 (two-tailed independent Student's t-test). Gene Ontology (GO) and Kyoto Encyclopedia of Genes and Genomes (KEGG) pathway enrichment analyses were performed using the DAVID bioinformatics resource (https://davidbioinformatics.nih.gov/). Gene set enrichment analysis (GSEA) was carried out using the online platform at cloud.oebiotech.cn/task/. For multi-omics integration analysis, phosphoproteins containing multiple differentially phosphorylated sites with consistent alteration trends were represented by the site with the largest absolute $\log_2$ fold change ($|\log_2 FC|$) among the corresponding regulated sites.

Isolation and culture of primary mouse thyroid epithelial cells

Primary thyroid epithelial cells were isolated from young and AR-SCH C57BL/6 mice. Briefly, mice were euthanized, and thyroid lobes were aseptically excised and immediately placed in ice-cold Hank's balanced salt solution (HBSS). After removal of surrounding connective tissue, the glands were minced into fragments of approximately 1 mm^3 and digested with 1 mg/mL collagenase type IV (Aladdin, C1509223) and 1 mg/mL dispase II (Aladdin, D1516122) in DMEM/F-12 medium at 37°C for 30-45 min with gentle agitation. The resulting cell suspension was gently triturated, filtered through a 70-μm cell strainer, and centrifuged at 400×g for 5 min. The cell pellet was resuspended in complete growth medium consisting of DMEM/F-12 supplemented with 10% fetal bovine serum (FBS), 1% penicillin-streptomycin, and 1 mU/mL TSH (MCE, HY-107916) to maintain the differentiated thyrocyte phenotype. Cells were maintained at 37°C in a humidified atmosphere of 5% CO_2. To minimize dedifferentiation *in vitro*, primary cells were used for experiments within 48-72 h of isolation without passaging.

Quantitative real-time PCR (qPCR)

Total RNA was extracted from cultured primary thyroid epithelial cells of young and AR-SCH mice (n = 6 per group) using TRIzol reagent (Aladdin, T751379) according to the manufacturer's instructions. RNA concentration and purity were assessed by the A260/A280 ratio, and 1 μg of total RNA was reverse-transcribed into cDNA. Quantitative real-time PCR was performed using SYBR Green master mix (Yeasen, 11184ES03) on a real-time PCR system, and each sample was analyzed in triplicate. The amplification specificity was verified by melting curve analysis. Relative mRNA expression levels were calculated using the $2^{-\Delta\Delta Ct}$ method, with GAPDH serving as the internal reference gene, and are expressed as fold change relative to the young group. Primer sequences are listed in Supplementary Table 1. Statistical comparisons between the two groups were performed using a two-tailed unpaired Student's

t-test, and *P*-value < 0.05 was considered significant.

Results

Characterization of histopathologic and serological phenotypes in aging thyroids

To establish the physiological and pathological baseline of thyroid senescence and validate the age-related subclinical hypothyroidism (AR-SCH) model, we first examined the histopathologic morphology and serum thyroid-related indices in young and AR-SCH mice. As 20-month-old mice exhibit distinct neuroendocrine variations equivalent to those of elderly humans, they were utilized here to characterize the molecular hallmarks of AR-SCH. Hematoxylin and eosin (H&E) histology revealed that thyroid tissues from the young mice maintained intact structural integrity and regular morphology, characterized by neatly arranged, colloid-filled thyroid follicles without signs of inflammatory infiltration (**Figure 1A**). In contrast, the aging mouse thyroids exhibited structural remodeling and tissue degeneration, manifesting as disordered follicular architecture, diminished follicular lumen volume, and noticeable infiltration of lymphocytes alongside extensive inflammatory cell aggregates (**Figure 1B**), which together indicated progressive senescent retrogressive changes and chronic inflammatory lesions within the AR-SCH thyroid [12, 23].

Serological profiles demonstrated altered neuroendocrine feedback loops and autoimmune activation during AR-SCH development. Crucially, biomarkers associated with thyroid autoimmunity and hormonal regulation were altered in the senescent cohort. While young mice exhibited negligible or basal expressions of TGAB, AR-SCH mice demonstrated a robust upregulation in serum TGAB levels (**Figure 1C**), aligning with an autoimmune-prone microenvironment [29, 30]. Quantifications of circulating thyroid hormones showed that serum thyroxine (T4) (**Figure 1D**) and triiodothyronine (T3) (**Figure 1E**) concentrations remained stable with no significant alterations between the two ages [29, 31]. However, corresponding to the latent functional decline, serum thyrotropin (TSH) levels in the AR-SCH mice displayed a compensatory and significant elevation compared to the low and steady baseline observed in the young mice (**Figure 1F**), consistent with the clinical feedback regulation observed in subclinical hypothyroidism [7, 8]. This state of elevated thyroid autoimmunity and modified protein localization was further substantiated at the tissue level by immunofluorescence staining, which revealed a prominent enhancement of thyroid peroxidase (TPO) protein expression within the thyroid follicles of AR-SCH mice relative to the young controls (**Figure 1G**, **1H**), confirming localized autoimmune activation accompanying AR-SCH progression [23].

Global proteomic profiling and differential expression analysis

We performed in-depth global proteomic profiling, including protein extraction, tryptic digestion, and label-free quantification, on thyroid tissues derived from 6 young and 6 AR-SCH mice using high-resolution mass spectrometry operating in data-independent acquisition (DIA) mode. This systematic analysis characterized the global protein expression dynamics during AR-SCH progression and provided a comprehensive molecular foundation for understanding age-related thyroid dysfunction.

In total, 6,666 proteins were identified across 12 thyroid samples. Of these, 6,002 proteins (90.04%) were quantifiable and detected in at least 60% of samples in either group, indicating high proteomic coverage and reliable quantification that capture the full protein expression landscape of young and AR-SCH mouse thyroids. Gene set enrichment analysis (GSEA) of the 6,002 quantified proteins revealed significant enrichment in AR-SCH mice for antigen processing and presentation (normalized enrichment score (NES) = 1.6, *P*-value = 0.01), cell adhesion molecules (NES = 1.74, *P*-value = 0.003), and autoimmune thyroid disease (NES = 1.55, *P*-value = 0.05) (**Figure 2A-C**) [3]. These enrichments demonstrated marked remodeling of immune regulation, cell-cell adhesion, and immune cell differentiation pathways during AR-SCH development [11, 15], consistent with the high prevalence of subclinical hypothyroidism in the elderly [4, 6-8, 29, 32].

Using thresholds of fold change (FC) > 1.5 or FC < 1/1.5 and *P*-value < 0.05, we identified 142 differentially expressed proteins (**Figure 2D**, **2E**). Of these, 26 proteins were upregulated, and 116 were downregulated in the AR-SCH group (81.69% downregulated) (**Figure**

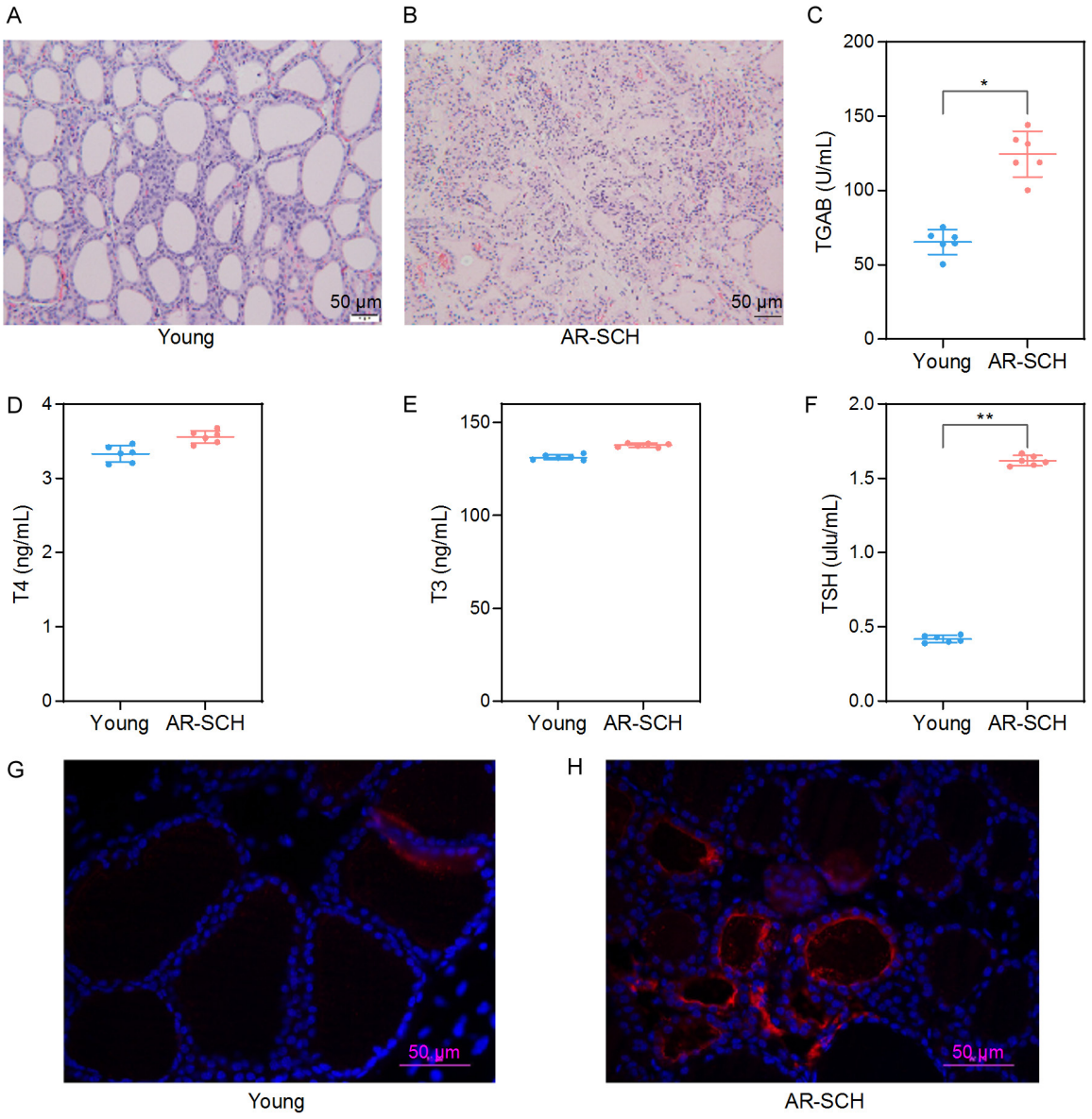

Figure 1. Histopathologic and serological landscapes of thyroid between the young and age-related subclinical hypothyroidism (AR-SCH) mice. (A, B) Hematoxylin-eosin (H&E) images of thyroid tissue sections derived from young (A) and AR-SCH mice (B) (Scale bars = 50 μm). (C-F) Quantitative analysis of the anti-thyroglobulin antibody (TGAB) (C), T4 (D), T3 (E), and serum thyrotropin (TSH) (F) concentrations between the young and AR-SCH thyroid. **P*-value < 0.05, ***P*-value < 0.01. Data are presented as mean ± standard deviation (SD), n = 6. (G, H) Immunofluorescence micrographs of thyroid peroxidase (TPO) expression (red) counterstained with 4',6-diamidino-2-phenylindole (DAPI, blue) in young (G) and AR-SCH (H) mouse thyroid tissues (Scale bars = 50 μm).

2F; Supplementary Data 1). This widespread downregulation of protein expression suggested that widespread loss of functional proteins underlies the structural degeneration and functional decline of the AR-SCH thyroid, in agreement with the notion that aging drives global attenuation of thyroid functional proteins [11, 13]. Functional enrichment analysis revealed proteins that were predominantly associated with cytoskeletal structural remodeling, stress fiber organization, and cellular architecture in thyroid epithelial cells (**Figure 2G-I**; Supplementary Data 2). Gene Ontology (GO) molecular functions further reflected widespread impairment of cytoskeletal anchoring and contractile properties. Concurrently, KEGG pathway enrich-

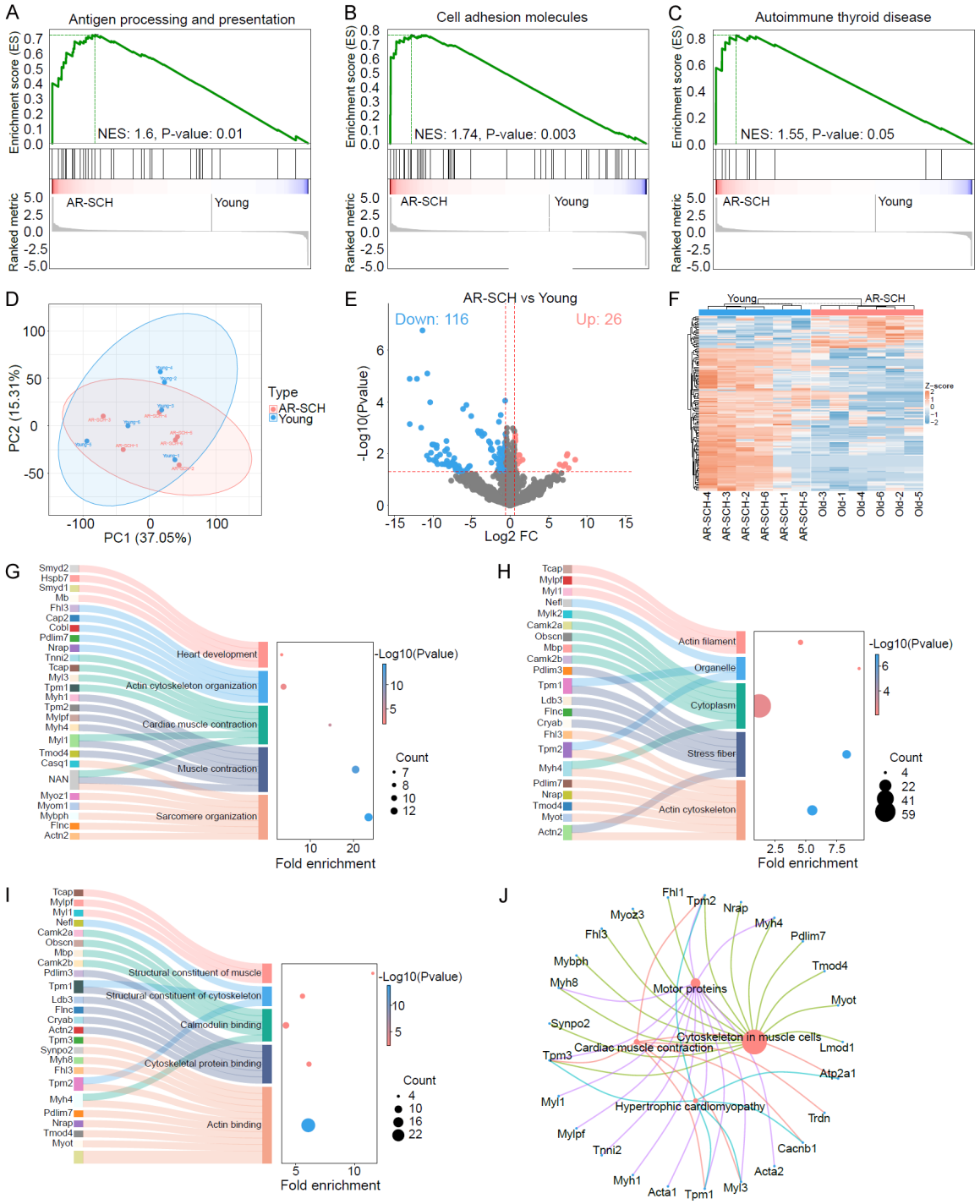

Figure 2. Global proteomic profiling and differential expression analysis of young and age-related subclinical hypothyroidism (AR-SCH) mouse thyroids. (A-C) Gene set enrichment analysis (GSEA) plots of the quantified proteins, including antigen processing and presentation (A), cell adhesion molecules (B), and autoimmune thyroid disease (C). (D) Principal component analysis (PCA) plot of the quantified proteome. (E) Volcano plot of the differentially expressed proteins between young and AR-SCH mice (thresholds: fold change > 1.5 or fold change < 1/1.5, *P*-value < 0.05). (F) Heatmap of the differentially expressed proteins. (G-J) Functional enrichment analysis of the down-regulated proteins, including Gene Ontology biological process (GO-BP) (G), GO-cellular component (GO-CC) (H), GO-molecular function (GO-MF) (I), and Kyoto Encyclopedia of Genes and Genomes (KEGG) (J).

ment in motor proteins, cardiac muscle contraction, and hypertrophic cardiomyopathy (**Figure 2J**; Supplementary Data 2) [9, 33, 34].

Phosphoproteomic profiling

We performed high-throughput identification and quantification of the thyroid phosphoproteome using the DIA method. After normalization to global protein abundance, we accurately mapped aging-related phosphorylation dynamics and revealed signaling network dysregulation in AR-SCH thyroid. Across 12 samples, we identified 3,284 phosphoproteins and 11,929 high-confidence phosphorylation sites (confidence > 0.75). In total, 2,374 phosphoproteins and 5,684 phosphorylation sites were quantified in ≥ 60% of samples per group, providing sufficient depth and precision for differential phosphoproteomic analysis. To exclude confounding effects of protein expression, we normalized phosphorylation-site intensities to global protein abundance, ensuring that differential phosphorylation reflected true changes in modification status.

Using FC > 1.5 or FC < 1/1.5 and *P*-value < 0.05, we identified 248 differentially phosphorylated sites: 21 upregulated and 227 downregulated (91.53% downregulated) in AR-SCH mice (**Figure 3A-C**; Supplementary Data 3). This extensive trend of hypophosphorylation indicated a widespread attenuation of signaling pathways during thyroid aging. Functional enrichment demonstrated that downregulated phosphoproteins were associated with impaired kinase activity, ATP binding, and focal adhesion, reflecting disrupted cytoskeletal anchoring and intracellular cellular architecture (**Figure 3D-F**; Supplementary Data 4). KEGG pathways analysis further linked these hypophosphorylated targets to motor proteins, actin cytoskeleton, apoptosis, and autophagy-animal cascades (**Figure 3G**; Supplementary Data 4). These findings suggest that altered phosphorylation status is associated with thyroid senescence-related changes through modulation of signaling networks involved in cell survival, autophagy-related processes, and structural stability [22-26, 35].

Site-specific N-glycan analysis

Using hydrophilic interaction chromatography (HILIC)-based enrichment, we performed the first comprehensive profiling of site-specific N-glycans in the aging mouse thyroid. We characterized glycosylation changes at four levels - N-glycoproteins, N-glycosites, N-glycans, and site-specific N-glycans - to reveal regulatory dynamics underlying AR-SCH and fill an important knowledge gap in aging-related glycoproteomic remodeling.

Across 12 samples, we identified 243 N-glycoproteins, 427 N-glycosites, 437 N-glycans, and 2,476 site-specific N-glycans. On average, each sample yielded 219 N-glycoproteins, 384 N-glycosites, 395 N-glycans, and 2,139 site-specific N-glycans, demonstrating deep and high-coverage N-glycoproteomic identification (**Figure 4A**). Enrichment specificity was defined as the proportion of MS/MS spectra containing ≥ 2 oxonium ions relative to total MS/MS spectra; the average N-glycosylation ratio was 40.99%, confirming high specificity and reliability of HILIC-based glycosylation enrichment in thyroid tissue (Supplementary Figure 1A).

Based on monosaccharide composition, site-specific N-glycans can be classified into three major types: oligomannose/high mannose (HM), sialylated N-glycans (Sia), and fucosylated N-glycans (Fuc). Fuc N-glycans dominated the thyroid glycan (61.36%), followed by Sia (20.31%) and HM (18.32%) (**Figure 4B**). Further stratification into both Fuc and Sia, free Fuc and Sia, only Fuc, and only Sia revealed that only Fuc was the most abundant subclass (43.74%), followed by free Fuc and Sia (36.87%) (**Figure 4C**). These data identified fucosylation as the primary N-glycosylation modification in mouse thyroid, likely governing immune homeostasis and cell recognition.

Site-specific N-glycans exhibited pronounced macro- and micro-heterogeneity. For macro-heterogeneity, 65.56% of N-glycoproteins carried a single N-glycosite, and 19.92% carried two N-glycosites, indicating predominant single-site N-glycosylation (**Figure 4D**). Analysis of N-glycan diversity per site showed that 35.68% of sites bore only one N-glycan and 29.88% bore > 4 N-glycans, highlighting the substantial complexity of site-specific glycosylation in the thyroid (Supplementary Figure 1B). For micro-heterogeneity, monofucosylation accounted for 72.48% (1,051/1,450) of fucosylated site-specific N-glycans (**Figure 4E**). Monosialylation represented 73.75% (354/480) of

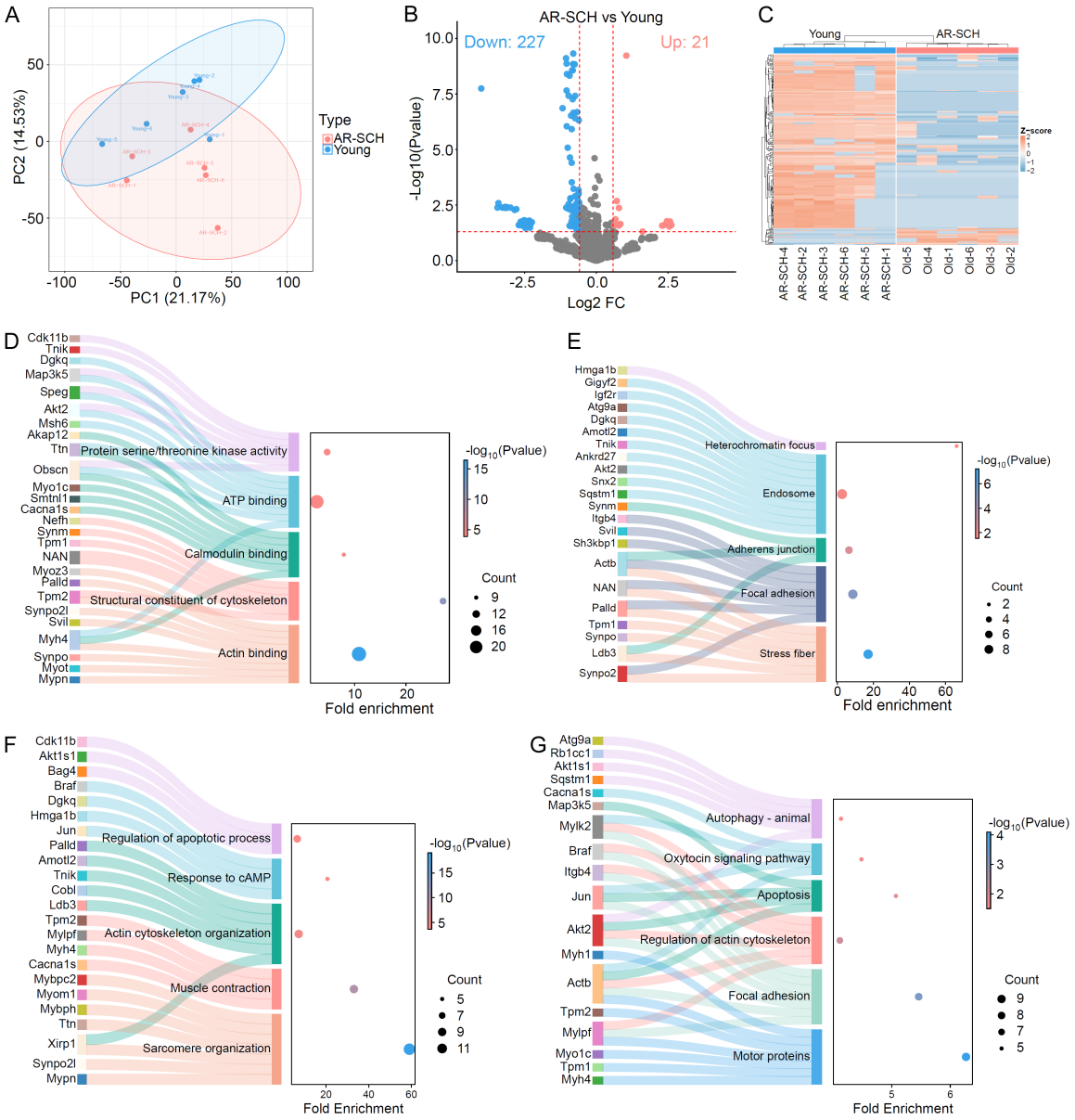

Figure 3. Phosphoproteomic profiling and dysregulated signaling networks in age-related subclinical hypothyroidism (AR-SCH) thyroid. (A) Principal component analysis (PCA) plot based on the quantified phosphorylation site intensities. (B) Volcano plot of quantified phosphorylation sites. (C) Heatmap of the differentially phosphorylated sites. (D-G) Functional enrichment analysis of the downregulated proteins, including Gene Ontology biological process (GO-BP) (D), GO-cellular component (GO-CC) (E), GO-molecular function (GO-MF) (F), and Kyoto Encyclopedia of Genes and Genomes (KEGG) (G).

sialylated site-specific N-glycans, with disialylation at 21.67% (104/480) (**Figure 4F**), defining the quantitative micro-heterogeneity pattern of thyroid glycosylation.

In total, 2320 site-specific N-glycans were quantified in ≥ 60% of samples per group. Principal component analysis (PCA) showed clear separation between young and AR-SCH groups, demonstrating global remodeling of the thyroid glycoproteome with aging (**Figure 4G**). To eliminate the confounding effects of protein abundance, we used N-glycan ratios at the same N-glycosite for differential analysis. We identified 1,182 differentially regulated site-specific N-glycans (FC > 1.5 or FC < 1/1.5, *P*-value < 0.05), including 567 upregulated and 615 downregulated site-specific N-glycans in

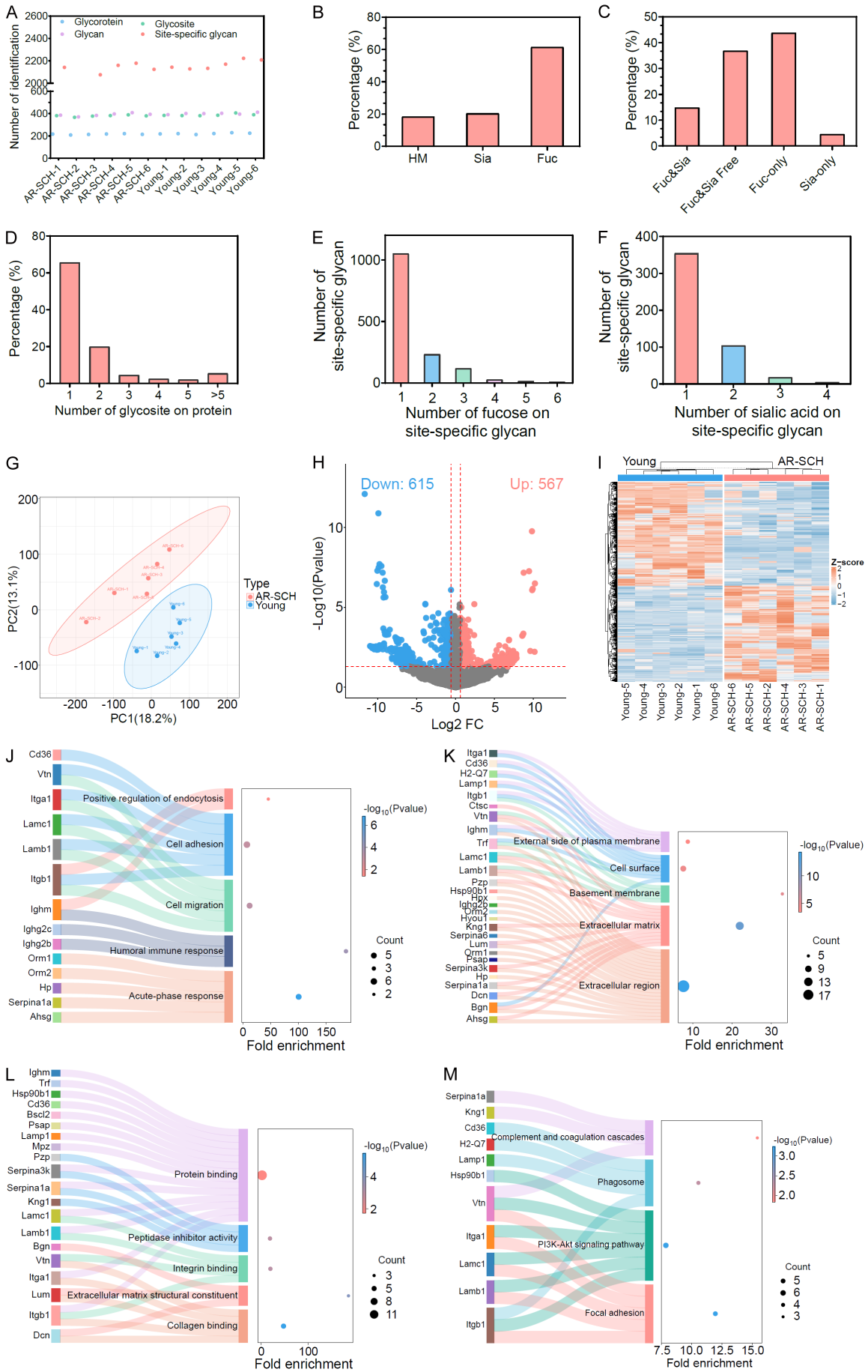
A
Number of identification
Glycoprotein
Glycan
Glycosite
Site-specific glycan
AR-SCH-1
AR-SCH-2
AR-SCH-3
AR-SCH-4
AR-SCH-5
AR-SCH-6
Young-1
Young-2
Young-3
Young-4
Young-5
Young-6
B
Percentage (%)
HM
Sia
Fuc
C
Percentage (%)
Fuc&Sia
Fuc&Sia Free
Fuc-only
Sia-only
D
Percentage (%)
Number of glycosite on protein
E
Number of site-specific glycan
Number of fucose on site-specific glycan
F
Number of site-specific glycan
Number of sialic acid on site-specific glycan
G
PC2(13.1%)
PC1(18.2%)
Type
AR-SCH
Young
H
Down: 615
Up: 567
-Log10(Pvalue)
Log2 FC
I
Young
AR-SCH
Z-score
J
Cd36
Vtn
Itga1
Lamc1
Lamb1
Itgb1
Ighm
Ighg2c
Ighg2b
Orm1
Orm2
Hp
Serpina1a
Ahsg
Positive regulation of endocytosis
Cell adhesion
Cell migration
Humoral immune response
Acute-phase response
-log10(Pvalue)
Count
Fold enrichment
K
Itga1
Cd36
H2-Q7
Lamp1
Itgb1
Ctsc
Vtn
Ighm
Trf
Lamc1
Lamb1
Pzp
Hsp90b1
Hpx
Ighg2b
Orm2
Hyou1
Kng1
Serpina6
Lum
Orm1
Psap
Serpina3k
Hp
Serpina1a
Dcn
Bgn
Ahsg
External side of plasma membrane
Cell surface
Basement membrane
Extracellular matrix
Extracellular region
-log10(Pvalue)
Count
Fold enrichment
L
Ighm
Trf
Hsp90b1
Cd36
Bscl2
Psap
Lamp1
Mpz
Pzp
Serpina3k
Serpina1a
Kng1
Lamc1
Lamb1
Bgn
Vtn
Itga1
Lum
Itgb1
Dcn
Protein binding
Peptidase inhibitor activity
Integrin binding
Extracellular matrix structural constituent
Collagen binding
-log10(Pvalue)
Count
Fold enrichment
M
Serpina1a
Kng1
Cd36
H2-Q7
Lamp1
Hsp90b1
Vtn
Itga1
Lamc1
Lamb1
Itgb1
Complement and coagulation cascades
Phagosome
PI3K-Akt signaling pathway
Focal adhesion
-log10(Pvalue)
Count
Fold enrichment

Figure 4. Comprehensive site-specific N-glycoproteomic remodeling in age-related subclinical hypothyroidism (AR-SCH) thyroid. (A) Overview of total identifications across 12 samples, including the numbers of N-glycoproteins, N-glycosites, N-glycans, and site-specific N-glycans. (B) The percentage distribution of the three major N-glycan types. (C) Distribution of detailed N-glycan subclasses. (D) Macro-heterogeneity profile evaluating the number of N-glycosites per protein. (E, F) Micro-heterogeneity distribution revealing the numbers of fucose residues (E) and sialic acid residues (F) per site-specific N-glycans. (G) Principal component analysis (PCA) plot based on the quantified site-specific N-glycans. (H) Volcano plot of the quantified site-specific N-glycans. (I) Heatmap of the differentially site-specific N-glycans. (J-M) Functional enrichment analysis of the proteins with downregulated site-specific N-glycans, including Gene Ontology biological process (GO-BP) (J), GO-cellular component (GO-CC) (K), GO-molecular function (GO-MF) (L), and Kyoto Encyclopedia of Genes and Genomes (KEGG) (M) enrichment of the downregulated site-specific N-glycans.

AR-SCH mice (**Figure 4H**, **4I**; Supplementary Data 5), establishing aberrant glycosylation as an important post-translational modification signature of AR-SCH pathology.

Functional enrichment analysis indicated that proteins carrying downregulated site-specific N-glycans were localized primarily to the extracellular matrix, basement membrane, and plasma membrane, associated with alterations in extracellular matrix structural organization and integrin binding (**Figure 4J-L**; Supplementary Data 6). KEGG pathways were significantly enriched in focal adhesion, PI3K-Akt signaling pathway, phagosome, and complement and coagulation cascades (**Figure 4M**; Supplementary Data 6) [19, 36-39].

Multi-omics integration

To dissect shared and distinct molecular changes across the global proteome, N-glycoproteome, and phosphoproteome in aging thyroid, Venn plots were generated for total quantified and differential proteins separately (**Figure 5A**, **5B**). At the total-protein level, 4,039, 45, and 844 proteins were uniquely detected in global, N-glyco, and phosphoproteome, respectively; 148 proteins overlapped between proteome and glycoproteome, 45 across all three datasets, and only 3 were shared solely by glycoproteome and phosphoproteome (**Figure 5A**). For differential molecules, very limited overlap was observed: just one shared altered protein existed between differential proteins and glycoproteins, with zero overlap between differential glycoproteins and phosphoproteins or across all three groups (**Figure 5B**). Such sparse intersection demonstrates protein expression, N-glycosylation and phosphorylation operate as largely independent regulatory axes in thyroid aging.

We further performed nine-quadrant correlation analysis using fold changes of total protein abundance and phosphorylation modification to decode their regulatory interplay. Of the 149 genes with significantly altered phosphorylation, 79.87% (119/149) showed unchanged total protein abundance; meanwhile, among 142 differentially expressed proteins, 78.87% (112/142) maintained stable phosphorylation levels (**Figure 5C**). Most molecules displayed synchronous downregulation of protein and phosphorylation, representing the dominant aging signature. Some genes (Ap4e1, Srcin1, Arhgap23, Alpk3) had steady protein levels but reduced phosphorylation, whereas rare candidates (Map3k2, Vps50, Tp53bp1) acquired elevated phosphorylation without altered protein abundance. Synchronously upregulated targets were scarce, and almost no genes exhibited increased protein alongside decreased phosphorylation. Such asynchronous regulation highlights the irreplaceable value of independent phosphoproteomic profiling.

Since differential N-glycan variation was defined via glycan ratios calculated at identical glycosites rather than absolute glycoprotein abundance, direct quantitative shifts of intact glycoproteins could not be readily obtained. Moreover, functional enrichment results of proteins carrying decreased site-specific N-glycans differed distinctly from those derived from global proteome and phosphoproteome datasets, indicating site-specific glycoproteomics supplies unique regulatory information unavailable from the other two omics layers.

Validation of candidate molecules and pathways

To validate experimentally the representative candidates identified by the multi-omics profiling at the cellular level, primary thyroid epithelial cells were isolated from young and AR-SCH mice, and qPCR analysis was performed. In line with the widespread downregulation of cytoskeletal and contractile proteins revealed by

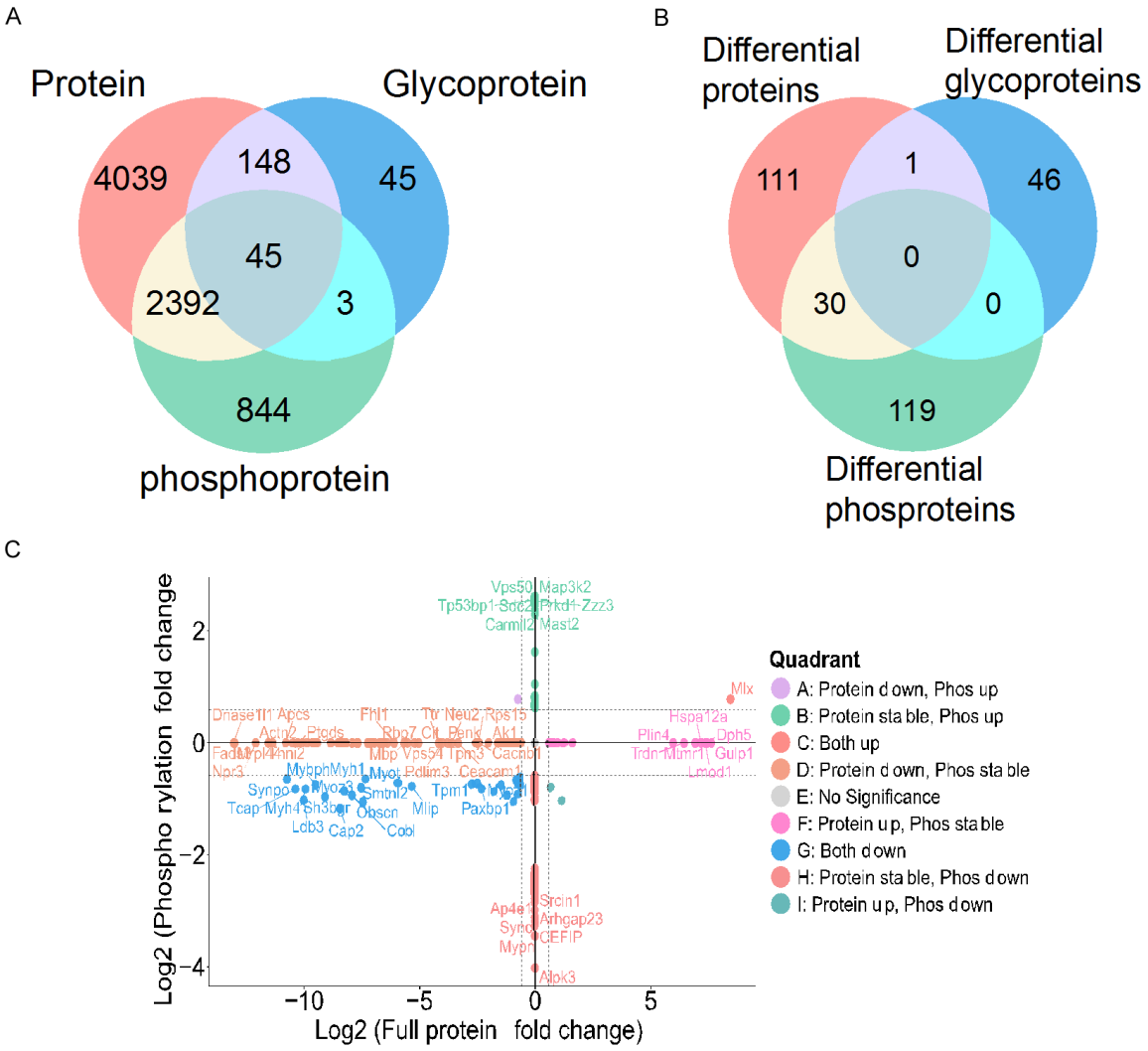

Figure 5. Multi-omics integrative landscape and regulatory correlation networks during age-related subclinical hypothyroidism (AR-SCH) development. (A, B) Venn diagrams displaying the degree of overlapping molecular targets among the global proteome, N-glycoproteome, and phosphoproteome, evaluated at the total quantified protein level (A) and the significantly differential molecule level (B). (C) Nine-quadrant scatter plot correlating the $\log_2$ fold changes of total protein abundance (x-axis) against the corresponding $\log_2$ fold changes of phosphorylation site intensity (y-axis).

global proteomics, the transcripts of the cytoskeletal constituents Actn1 and Tpm1 were markedly decreased in AR-SCH-derived thyrocytes compared with young controls (**Figure 6A** and **6F**), corroborating the age-related collapse of the cytoskeletal architecture. Regarding the autophagy-related candidates highlighted by the phosphoproteomic analysis, the expression of Sqstm1 (p62) was significantly increased, whereas Map1lc3b (LC3B) was downregulated in AR-SCH-derived cells (**Figure 6C** and **6D**), supporting compromised autophagic clearance during thyroid aging. Moreover, Fut8, the core fucosyltransferase underlying the aberrant fucosylation identified by site-specific N-glycoproteomics, was significantly downregulated (**Figure 6B**). Finally, in agreement with the extensive hypophosphorylation of intracellular signaling cascades, the relative level of p-AKT/AKT was reduced in AR-SCH-derived thyrocytes (**Figure 6E**).

Immunofluorescence staining of the primary thyrocytes further verified these alterations at the protein level (**Figure 6G**). Cleaved caspase-3 immunofluorescence was markedly str-

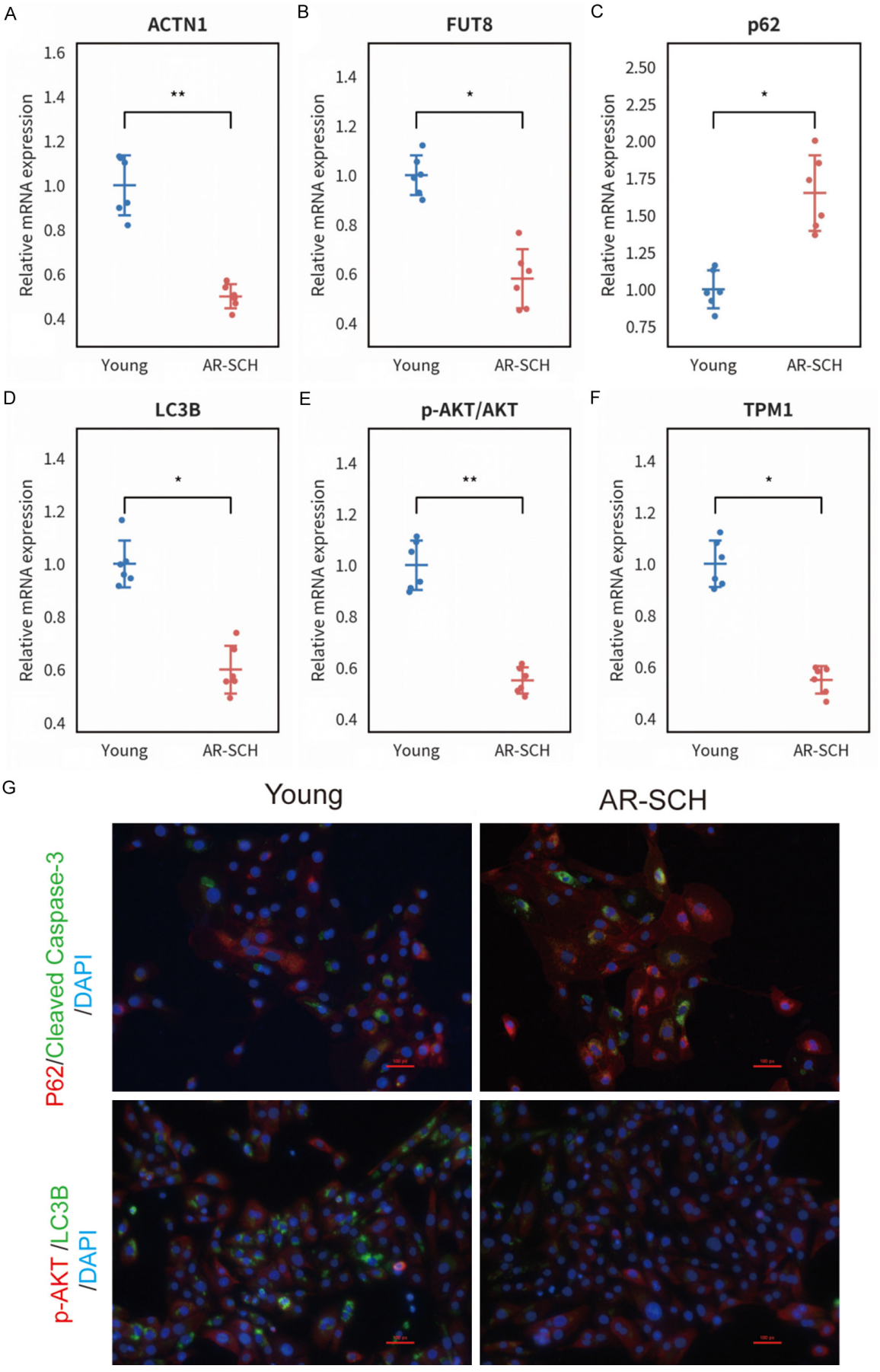
A
ACTN1
Relative mRNA expression
1.6
1.4
1.2
1.0
0.8
0.6
0.4
**
Young
AR-SCH
B
FUT8
Relative mRNA expression
1.4
1.2
1.0
0.8
0.6
0.4
*
Young
AR-SCH
C
p62
Relative mRNA expression
2.50
2.25
2.00
1.75
1.50
1.25
1.00
0.75
*
Young
AR-SCH
D
LC3B
Relative mRNA expression
1.4
1.2
1.0
0.8
0.6
0.4
*
Young
AR-SCH
E
p-AKT/AKT
Relative mRNA expression
1.4
1.2
1.0
0.8
0.6
0.4
**
Young
AR-SCH
F
TPM1
Relative mRNA expression
1.4
1.2
1.0
0.8
0.6
0.4
*
Young
AR-SCH
G
Young
AR-SCH
P62/Cleaved Caspase-3
/DAPI
p-AKT /LC3B
/DAPI

Figure 6. Validation of representative candidate molecules and pathways in primary thyrocytes from young and age-related subclinical hypothyroidism (AR-SCH) mice. (A-F) Relative mRNA expression levels of Actn1 (A), Fut8 (B), Sqstm1 (p62) (C), Map1lc3b (LC3B) (D), p-AKT/AKT (E), and Tpm1 (F) in primary thyroid epithelial cells isolated from young and AR-SCH mice, determined by quantitative real-time PCR. **P*-value < 0.05, ***P*-value < 0.01 (two-tailed unpaired Student's t-test). (G) Representative immunofluorescence images of primary thyrocytes from young and AR-SCH mice co-stained for p62 (red) and cleaved caspase-3 (green) (upper panels), and for p-AKT (red) and LC3B (green) (lower panels); nuclei were counterstained with 4',6-diamidino-2-phenylindole (DAPI). Scale bars = 100 μm.

onger in AR-SCH-derived thyrocytes than in young cells, indicating enhanced apoptotic activation at the cellular level. Concomitantly, p62 accumulated prominently in the cytoplasm of AR-SCH-derived cells, whereas LC3B staining was attenuated, together indicating compromised autophagic clearance in senescent thyroid cells. In agreement with the global hypophosphorylation revealed by the phosphoproteomic analysis, p-AKT immunoreactivity, which was abundant in young thyrocytes, was substantially diminished in AR-SCH-derived cells, directly corroborating the suppression of AKT-mediated signaling. Collectively, the qPCR and immunofluorescence results obtained in primary thyrocytes provide experimental validation, at both the transcript and protein levels, for the representative candidates derived from each omics layer and reinforce the proposed mechanistic framework in which cytoskeletal collapse, signaling attenuation, autophagic decline, and aberrant fucosylation jointly drive AR-SCH progression.

Discussion

Using an integrated strategy combining global proteomics, site-specific N-glycoproteomics, and phosphoproteomics, we characterized molecular alterations associated with AR-SCH in mice. We suggest that cytoskeletal remodeling, altered immune dysregulation, signaling attenuation, and shifting apoptosis/autophagy balances collectively characterize age-related thyroid hypofunction. These changes suggest that remodeling of cytoskeletal and contractile constituents is a prominent structural feature of the aging thyroid [4, 6].

The observed histopathologic degeneration, characterized by prominent lymphocytic infiltration and elevated autoimmune antibody titers (**Figure 1**), closely aligns with the widespread immunologic and structural remodeling unveiled by our multi-omics profiling [1, 11, 29]. Specifically, enrichment of antigen processing and presentation and autoimmune thyroid disease in GSEA (**Figure 2**) is consistent with the immune-related changes observed in senescent thyroids [11]. Concurrently, age-related changes in actin-cytoskeleton and stress-fiber components are consistent with the architectural disruption and reduced follicular lumen observed by H&E imaging, suggesting coordinated structural alterations during thyroid aging [12].

Global proteomic profiling revealed a widespread downregulation of functional proteins, strongly enriched for cytoskeletal and contractile pathways. These changes support an association between altered cytoskeletal and contractile structures pathways and structural remodeling in the aging thyroid. Because cytoskeletal organization is important for follicle morphology, hormone storage, and secretion, the observed age-related changes may be relevant to follicular atrophy and altered colloid handling. Concurrently, enrichment of cardiac contractile pathways may reflect systemic or cross-tissue associations relevant to the reported relationship between hypothyroidism and cardiovascular risk; this possibility requires dedicated functional investigation [9, 10, 33].

Site-specific N-glycoproteomic profiling identified fucosylation as the dominant and dysregulated glycan feature in aging thyroid. Downregulated N-glycosylation targeted pathways governing humoral immunity, cell adhesion, and complement activation, primarily localized to the extracellular matrix and cell surface. As an important regulator of immune recognition and cell adhesion, aberrant glycosylation impairs local immune surveillance and follicular epithelial integrity, promoting autoimmunity. These results identify glycosylation remodeling as a potential molecular feature linking aging with thyroid immune-related changes [3, 19, 20, 38, 39].

Phosphoproteomic analysis uncovered global hypophosphorylation in the AR-SCH thyroid, affecting focal adhesion, actin cytoskeleton

regulation, apoptosis, and autophagy pathways [16]. As a regulatory element for intracellular signaling, widespread hypophosphorylation is associated with pathways related to repair signaling, apoptosis, and autophagy. These findings match conserved aging-related hypophosphorylation and autophagic decline and provide molecular targets for apoptosis-inhibitory strategies to ameliorate age-related subclinical hypothyroidism [22, 23, 35, 38].

Integrated analysis of the global proteome, site-specific N-glycoproteome, and phosphoproteome revealed a unified molecular network underlying thyroid aging. At the proteome level, core declines occurred in cytoskeletal and cardiac contractile proteins, consistent with thyroid hormone regulation of sarcopenia and myopathies [34, 40]. Glycosylation was defined by aberrant fucosylation and downregulated glycosylation of immune and extracellular matrix proteins, supporting a central role for glycosylation in thyroid physiology and disease [17, 19]. Phosphorylation was characterized by suppressed signaling and cytoskeletal phosphorylation, with activation of apoptotic and autophagic pathways, aligning with conserved mechanisms of organ aging [18]. Collectively, multi-omics data highlight cytoskeletal structural variations, immunological homeostasis shifts, enhanced apoptosis, and modified thyroid-heart crosstalk as prominent molecular features of age-related thyroid decline, providing a multi-layered resource for mechanistic and translational studies of subclinical hypothyroidism in the elderly.

Conclusions

Coordinated proteomic, glycoproteomic, and phosphoproteomic alterations were noted in aging thyroids, including changes related to cytoskeletal organization, immune-related processes, and signaling pathways.

Data availability

The proteomics data generated in this study are available through the ProteomeXchange Consortium via the iProX partner repository under the accession number PXD080737 [41, 42].

Disclosure of conflict of interest

None.

Address correspondence to: Qing Zhou, Department of Ophthalmology, Children's Hospital of Nanjing Medical University, 72 Guangzhou Road, Gulou District, Nanjing 210008, Jiangsu, China. E-mail: qingzhou112@sina.com

References

[1] Hao X, Du L, Liu G, Li Z and Wang S. Human retinal organoids for modelling dry age-related macular degeneration and screening drugs. Genes Dis 2025; 12: 101593.

[2] Ullah A, Singla RK, Cao D, Chen B and Shen B. Age-related and postmenopausal breast cancer progression and treatment management: the significance of pro-inflammatory cytokines and CXC chemokines. Genes Dis 2025; 12: 101606.

[3] Chen Z, Li M, Feng Y, Chen Y, Cai Z, Xu Y and Pang R. Identification and analysis of immune aging related biomarkers in cartilage and meniscus tissues of osteoarthritis. Am J Clin Exp Immunol 2025; 14: 204-222.

[4] Gesing A, Lewiński A and Karbownik-Lewińska M. The thyroid gland and the process of aging; What is new? Thyroid Res 2012; 5: 16.

[5] Zou Z and Zhong L. Anaplastic thyroid cancer: genetic roles, targeted therapy, and immunotherapy. Genes Dis 2024; 12: 101403.

[6] Leng O and Razvi S. Hypothyroidism in the older population. Thyroid Res 2019; 12: 2.

[7] Xu Y, Hysaj O, Qi X, Feller M, Pingitore A, Brown SJ, Ittermann T, Iacoviello M, Trompet S, Han JW, Schmidt B, Sgarbi JA, Valdés S, Muendlein A, Riis J, Andersen S, Drexel H, Teumer A, Dörr M, Vanderpump MPJ, Wareham N, Vaes B, Visser WE, Jukema JW, Imaizumi M, Dullaart RPF, Medici M, Fink HA, Ceresini G, Ferrucci L, Ikram MA, Hankey GJ, Iervasi G, Eastell R, Bauer DC, Williams GR, Boelaert K, Psaty BM, Führer-Sakel D, Bakker SJL, Kiemeney LALM, Riksen NP, Kim KW, Azizi F, Völzke H, Yeap BB, Razvi S, Gussekloo J, Walsh JP, Bensenor IM, Mammen J, Rodondi N, Cappola AR, Peeters RP and Chaker L; Thyroid Studies Collaboration. Natural history of thyroid function in ageing: an individual participant data analysis of 137 488 participants from 31 prospective cohort studies. Lancet Diabetes Endocrinol 2026; 14: 485-497.

[8] Fu J, Wang Y, Liu Y, Song Q, Cao J and Peichang W. Reference intervals for thyroid hormones for the elderly population and their influence on the diagnosis of subclinical hypothyroidism. J Med Biochem 2023; 42: 258-264.

[9] Olanrewaju OA, Asghar R, Makwana S, Yahya M, Kumar N, Khawar MH, Ahmed A, Islam T, Kumari K, Shadmani S, Ali M, Kumar S, Khatri M, Varrassi G and Mohamad T. Thyroid and its ripple effect: impact on cardiac structure,

function, and outcomes. Cureus 2024; 16: e51574.
[10] Xu Y, Licher S, Visser WE, Bakker SJL, Peeters RP, Dullaart RPF and Chaker L. Thyroid function and all-cause mortality in the context of multimorbidity: results from 2 population-based studies. J Clin Endocrinol Metab 2026; 111: e390-e397.
[11] Franceschi C, Ostan R, Mariotti S, Monti D and Vitale G. The aging thyroid: a reappraisal within the geroscience integrated perspective. Endocr Rev 2019; 40: 1250-1270.
[12] Liu CL, Chien MN, Hsu YC and Cheng SP. Transcriptomic characteristics associated with aging in the thyroid gland. Front Nutr 2022; 9: 859702.
[13] Scifo E, Morsy S, Liu T, Xie K, Schaaf K, Bano D and Ehninger D. Proteomic aging signatures across mouse organs and life stages. EMBO J 2025; 44: 4631-4660.
[14] Lu H, Liu X, Zhou Q, Li R, Zuo H, Hu K, Tian M, Wang H, Li J, Li N and Hou S. Integrated analysis of single-cell RNA-seq and ATAC-seq in lens epithelial cells: unveiling the role of ATF6 as a key transcription factor. Genes Dis 2025; 12: 101610.
[15] Takasugi M, Nonaka Y, Takemura K, Yoshida Y, Stein F, Schwarz JJ, Adachi J, Satoh J, Ito S, Tombline G, Biashad SA, Seluanov A, Gorbunova V and Ohtani N. An atlas of the aging mouse proteome reveals the features of age-related post-transcriptional dysregulation. Nat Commun 2024; 15: 8520.
[16] Li Y, Wang B, Zheng Y, Kang H, He A, Zhao L, Guo N, Liu H, Mardinoglu A, Mamun MAA, Gao Y and Chen X. The multifaceted role of post-translational modifications of LSD1 in cellular processes and disease pathogenesis. Genes Dis 2024; 12: 101307.
[17] Zhang Y, Zhou T, Tang Q, Feng B and Liang Y. Identification of glycosyltransferase-related genes signature and integrative analyses in patients with ovarian cancer. Am J Clin Exp Immunol 2024; 13: 12-25.
[18] Zhou T, Cao J, Tang Q, Jin J, Liang Y and Feng B. Exploring the role of Naa40 in immune infiltrates and prognostic prediction in hepatocellular carcinoma. Am J Clin Exp Immunol 2024; 13: 26-34.
[19] Ząbczyńska M, Kozłowska K and Pocheć E. Glycosylation in the thyroid gland: vital aspects of glycoprotein function in thyrocyte physiology and thyroid disorders. Int J Mol Sci 2018; 19: 2792.
[20] Martin TC, Šimurina M, Ząbczyńska M, Martinic Kavur M, Rydlewska M, Pezer M, Kozłowska K, Burri A, Vilaj M, Turek-Jabrocka R, Krnjajić-Tadijanović M, Trofimiuk-Müldner M, Ugrina I, Lityńska A, Hubalewska-Dydejczyk A, Trbojevic-Akmacic I, Lim EM, Walsh JP, Pocheć E, Spector TD, Wilson SG and Lauc G. Decreased immunoglobulin G core fucosylation, a player in antibody-dependent cell-mediated cytotoxicity, is associated with autoimmune thyroid diseases. Mol Cell Proteomics 2020; 19: 774-792.
[21] Li W, Fan D, Wei D, Wei W, Zhang Y and Yi M. Causal relationship between IgG N-glycosylation and autoimmune thyroid diseases, and the possible mediating role of immune cells and inflammatory cytokines. Medicine (Baltimore) 2025; 104: e45649.
[22] Aman Y, Schmauck-Medina T, Hansen M, Morimoto RI, Simon AK, Bjedov I, Palikaras K, Simonsen A, Johansen T, Tavernarakis N, Rubinsztein DC, Partridge L, Kroemer G, Labbadia J and Fang EF. Autophagy in healthy aging and disease. Nat Aging 2021; 1: 634-650.
[23] Zong D, Sun B, Ye Q, Cao H and Guan H. Circadian gene BMAL1 regulation of cellular senescence in thyroid aging. Aging Cell 2025; 24: e70119.
[24] Hu X and Zhou Y. Curcumin reduces methionine adenosyltransferase 2b expression by interrupting phosphorylation of P38 MAPK in hepatic stellate cells. Eur J Pharmacol 2020; 886: 173424.
[25] Wang G, Joel MDM, Yuan J, Wang J, Cai X, Ocansey DKW, Yan Y, Qian H, Zhang X, Xu W and Mao F. Human umbilical cord mesenchymal stem cells alleviate inflammatory bowel disease by inhibiting ERK phosphorylation in neutrophils. Inflammopharmacology 2020; 28: 603-616.
[26] Sun L, Wang X, Gu T, Hu B, Luo J, Qin Y and Wan C. Nicotine triggers islet B cell senescence to facilitate the progression of type 2 diabetes. Toxicology 2020; 441: 152502.
[27] Dong W, Chen L, Jia L, Chen Z, Shen J, Li P and Sun S. Maximal performance of intact N-glycopeptide enrichment using sequential HILIC and MAX columns. Anal Bioanal Chem 2023; 415: 6431-6439.
[28] Zhou H, Ye M, Dong J, Corradini E, Cristobal A, Heck AJ, Zou H and Mohammed S. Robust phosphoproteome enrichment using monodisperse microsphere-based immobilized titanium (Iv) ion affinity chromatography. Nat Protoc 2013; 8: 461-480.
[29] Van Heemst D. Thyroid dysfunction in ageing populations. Endocr Connect 2025; 14: e250185.
[30] Yang D, Lu C, Zhang H, Shi X, Sun Y, Shao Y, Fan S, Tian L and Teng D. Assessing thyroid health: phenotypic age compared to chronological age. Front Endocrinol (Lausanne) 2025; 16: 1594139.
[31] Razvi SS, Wild H, Ingoe L, Vernazza J, Vanderpump M, Pearce SHS and Ludgate M. Changes

in thyroid function and autoimmunity in older individuals: longitudinal analysis of the whickham cohort. J Clin Endocrinol Metab 2025; 110: e3078-e3084.
[32] Lu J, Tang CM, Ge GM, Cheng KK, Lee KC, Tan KC, Lam SK, Cheung EY, Cheung CL and Li GH. Application of age- and sex-specific reference intervals for thyroid-stimulating hormone and free thyroxine in evaluating incidence and trends of thyroid dysfunctions: a population-based cohort study. BMC Med 2026; 24: 395.
[33] Grais IM and Sowers JR. Thyroid and the heart. Am J Med 2014; 127: 691-698.
[34] Dillmann WH. Cellular action of thyroid hormone on the heart. Thyroid 2002; 12: 447-452.
[35] Lim SHY, Hansen M and Kumsta C. Molecular mechanisms of autophagy decline during aging. Cells 2024; 13: 1364.
[36] Maverakis E, Kim K, Shimoda M, Gershwin ME, Patel F, Wilken R, Raychaudhuri S, Ruhaak LR and Lebrilla CB. Glycans in the immune system and the altered glycan theory of autoimmunity: a critical review. J Autoimmun 2015; 57: 1-13.
[37] Xu Y, Huo J, Nie R, Ge L, Xie C, Meng Y, Liu J, Wu L and Qin X. Altered profile of glycosylated proteins in serum samples obtained from patients with Hashimoto's thyroiditis following depletion of highly abundant proteins. Front Immunol 2023; 14: 1182842.
[38] Zhu S, Wu Q, Zhang B, Wei H, Li B, Shi W, Fang M, Zhu S, Wang L, Lang Zhou Y and Dong Y. Autophagy-related gene expression classification defines three molecular subtypes with distinct clinical and microenvironment cell infiltration characteristics in colon cancer. Int Immunopharmacol 2020; 87: 106757.
[39] Xu X, Su YL, Shi JY, Lu Q and Chen C. Microrna-17-5p promotes cardiac hypertrophy by targeting Mfn2 to inhibit autophagy. Cardiovasc Toxicol 2021; 21: 759-771.
[40] Matheny CJ, Qadota H, Bailey AO, Valdebenito-Silva S, Oberhauser AF and Benian GM. The myosin chaperone Unc-45 has an important role in maintaining the structure and function of muscle sarcomeres during adult aging. Mol Biol Cell 2024; 35: ar98.
[41] Chen T, Ma J, Liu Y, Chen Z, Xiao N, Lu Y, Fu Y, Yang C, Li M, Wu S, Wang X, Li D, He F, Hermjakob H and Zhu Y. iProX in 2021: connecting proteomics data sharing with big data. Nucleic Acids Res 2022; 50: D1522-D1527.
[42] Ma J, Chen T, Wu S, Yang C, Bai M, Shu K, Li K, Zhang G, Jin Z, He F, Hermjakob H and Zhu Y. iProX: an integrated proteome resource. Nucleic Acids Res 2019; 47: D1211-D1217.

Supplementary Table 1. Primer sequences used for quantitative PCR

Target	Gene symbol	Forward primer (5'-> 3')	Reverse primer (5'-> 3')
p-AKT/AKT	Akt1	AGAAGAGACGATGGACTT	GCTTCAGGTACTCAAACT
LC3B	Map1lc3b	CGTCCTGGACAAGACCAAGT	TCCGTCCTTCGCTTCATAGG
p62	Sqstm1	ACAGCCAGAGGAACAGATGG	GTAGAGACTGGAGTTCACCTGTA
FUT8	Fut8	CCTCAGTCAAACAGATGGAGCAG	ACACCAGCTTCCTGGCTTTGCT
ACTN1	Actn1	TCGCCAAGTGTCAACGCTCGTT	GGTCGATGGTTTCCAGCAGCTT
TPM1	Tpm1	TGAGCAAGCGGAGGCTGATAAG	GCATCTTTGAGAGCCTCGGAGT
	Gapdh	AAGAGGGATGCTGCCCTTAC	CGGGACGAGGAAACACTCTC

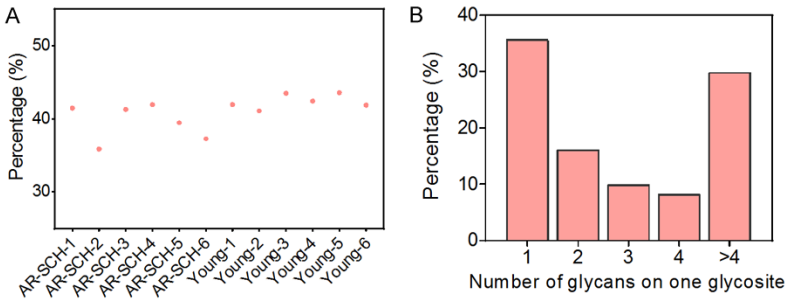

Supplementary Figure 1. Characterization of N-glycoproteome in mouse thyroids. A. Enrichment specificity across 12 individual thyroid samples from the young control and AR-SCH cohorts. B. Percentage distribution of the number of glycan compositions attached through individual N-glycosylation.